Research on Power Factor Improvement of a PM Vernier In-wheel Motor with Collaborative Design of PM and Armature Flux Linkage

Zixuan Xiang, *Member, IEEE*, Lei Peng, Xiaoyong Zhu, *Member, IEEE*, Jiaqiang Wei, and Zhe Yue

***Abstract*—This paper proposes a collaborative design method for enhancing the power factor and torque of electric motors. First, the intrinsic relationship between flux linkage analysis of the permanent magnet (PM) and armature field and the power factor is explored. Then, the connection between flux linkage and harmonics is established, clarifying the mechanism for improving power factor and torque. Improvements are focused on the PM and permeance. Regarding the PM structure, employing a Y-shaped PM structure effectively increases PM utilization, reduces leakage flux at the outer ends, and enhances the PM flux linkage. Concerning permeance, stator tooth design is optimized to cooperatively improve permeance harmonics, reduce the non-working flux linkage of the armature field, and enhance the fundamental modulation wave of the armature field responsible for torque generation. This improves the power factor while maintaining motor torque. Finally, through PM structural design, the motor torque performance is optimized. Furthermore, the performance of the Y-shaped PM motor is evaluated. A prototype was manufactured and tested. Theoretical analysis and experimental results demonstrate the effectiveness of the proposed method to a significant extent.**

***Index Terms*—Permanent magnet vernier motor, Flux linkage, Power factor, Torque**

I. INTRODUCTION

In recent years, permanent magnet vernier machines (PMVMs) have attracted increasing attention due to their magnetic field modulation effect, which provides higher torque density than conventional permanent magnet (PM) machines. This characteristic makes PMVMs potential candidates for direct-drive applications such as distributed-drive electric vehicles, marine propulsion, and cranes [1]-[5].

Although PM vernier motors offer the advantage of high torque density, their low power factor, attributable to leakage flux and high inductance, necessitates the use of bulky power converters during operation. This significantly increases the operational cost of the motor [6]-[10].

The large inductance in PM vernier motor is primarily caused by the high-modulation armature field. When the motor employs the d-axis current $I_d = 0$ control, the flux linkage is proportional to the inductance. Improving the power factor can thus be approached via the flux linkage [11]-[15].

To address this situation, some scholars have improved the motor power factor by enhancing the PM flux linkage and suppressing the armature flux linkage [16]-[17]. First, by utilizing the flux concentration effect to increase the PM flux linkage, numerous PM topological structures have been proposed. Examples include spoke-type, V-shaped, and Halbach configurations [18]-[20]. Owing to the flux concentration effect, these PM topologies enhance the average torque but offer limited improvement to the power factor. Other studies have improved the power factor by weakening inductance and suppressing armature flux linkage. In [21], to avoid harmonic leakage inductance caused by low-order harmonics, stator magnetic barriers were designed to increase the power factor. In [22], a dual-stator structure was adopted; since the magnetic circuits of the inner and outer stators are in series, their leakage flux is reduced, thereby improving the power factor. In [23], a yokeless Halbach array was proposed to suppress inductance, leading to power factor improvement.

The airgap serves as a critical conduit for energy transmission, and its magnetic flux density distribution directly influences motor performance. Airgap magnetic field harmonics offer a novel perspective for the analysis of PMVMs [24]-[26]. In [27], collaborative optimization of both PM harmonics and armature harmonics effectively enhanced motor power factor. Reference [28] examined power factor and torque through coordinated investigation of armature and PM field harmonics. By identifying and selectively optimizing harmonics contributing to torque and power factor across both fields, simultaneous improvement in torque and power factor was achieved. These studies demonstrate that harmonic analysis facilitates establishing torque-power factor correlations, enabling more targeted power factor enhancements. The distribution of airgap magnetic fields is primarily determined by three key elements of magnetic field modulation theory: magnetic source, permeance, and filter element [29]-[31]. Building upon this foundation, this paper conducts an analysis from the perspective of airgap harmonics. By leveraging magnetic source and permeance

Manuscript received August 12, 2025; revised October 20, and December 23, 2025; accepted January 09, 2026. Date of publication March 25, 2026; Date of current version January 16, 2026.

Zixuan Xiang, Lei Peng, Xiaoyong Zhu, Jiaqiang Wei, and Zhe Yue are with the School of Electrical and Information Engineering, Jiangsu University, Jiangsu 212013, China (e-mail: zxxiang@ujs.edu.cn; 2212307004@stmail.ujs.edu.cn; zxyff@ujs.edu.cn; 2210107011@stmail.ujs.edu.cn; 2222307074@stmail.ujs.edu.cn).

(*Corresponding author*: *Zixuan Xiang*)

Digital Object Identifier 10.30941/CESTEMS.2026.00001

design approaches, collaborative improvement of both power factor and torque is realized.

The remainder of this paper is organized as follows. Section II analyzes key harmonics influencing power factor and torque from perspectives of both PM and armature fields. Section III determines the topology and structural design ranges for magnetic sources while implementing targeted improvements for armature field harmonics through permeance design. PM structural design is subsequently executed to compensate for the torque harmonic reduction caused by permeance design. This integrated approach ultimately achieves synergistic improvement in power factor and torque. Section IV details electromagnetic performance characteristics of the Y-shaped PM motor. Section V covers motor fabrication and experimental validation. Finally, Section VI concludes the paper.

II. STRUCTURE AND ANALYSIS OF WORKING HARMONICS

For PM vernier motor, the airgap serves as the critical channel for energy conversion; its magnetic field harmonic distribution directly influences motor performance. Furthermore, the airgap magnetic field is composed of the superposition between the PM field and the armature field. Consequently, investigating the specific effects of harmonics from these two magnetic fields on power factor and torque contributes to motor performance improvement. The design methodology for this motor is illustrated in Fig. 1, primarily consisting of two components: the magnetic source and the modulation teeth. Regarding the magnetic source, changes in the PM topology enhance the fundamental amplitude produced by the PMs, strengthen the working harmonics, and thereby increase the motor PM flux linkage. Concerning the modulation teeth, the distribution of stator permeance harmonics is modified to further improve both the PM flux linkage and the armature flux linkage. Through these two-part designs, improvement in the motor magnetic field is achieved, thereby enhancing the motor power factor and torque performance.

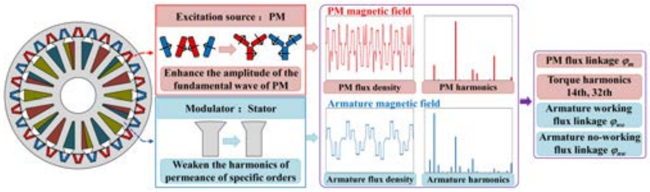

Fig. 1. Conceptual picture of enhancing power factor and torque between magnetic source and permeance in motor.

A. Motor Topology

The topology of the initial motor is presented in Fig. 2. Its PMs employ a V-shaped topology, which exhibits a stronger flux concentration effect. The PM field within the motor is enhanced, granting the motor higher torque output capability. This motor utilizes a 28-pole 18-slot pole-slot combination. Open slots enable the stator to function as modulation units, introducing magnetic field modulation effects into the machine. The motor employs fractional-slot windings with a coil pitch of 2. Distributed windings generate back electromotive force with lower harmonic content than concentrated windings.

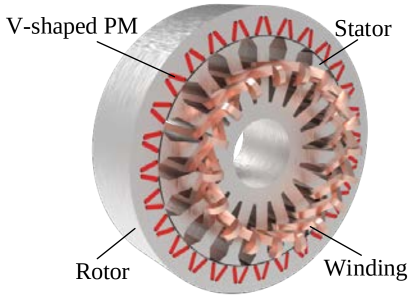

Fig. 2. The picture of initial motor topology.

B. Analysis of Power Factor and Torque from PM and Armature Fields

Furthermore, to facilitate power factor calculation, Fig. 3 illustrates the motor voltage phasor diagram when $I_d = 0$ control is adopted; under this condition, the inductance components are entirely substituted by flux linkages. In the diagram, U and ω_m represent the motor phase voltage and frequency, respectively; E_0 represents the fundamental back-electromotive force (back-EMF); φ_m denotes the PM flux linkage; φ_{wo} and φ_{nw} represent the armature working flux linkage and non-working flux linkage, respectively; φ_σ signifies the leakage flux linkage; θ_p represents the power factor angle.

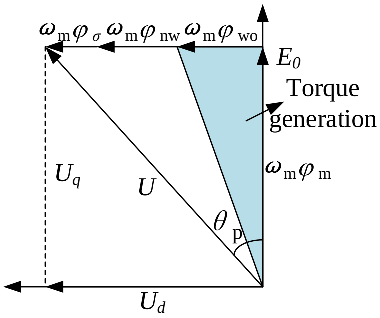

Fig. 3. Voltage phasor diagram of the motor under $I_d = 0$ control.

Therefore, according to Fig. 3, the power factor expression of the motor is expressed as (1):

$$\cos\theta_p = \frac{E_0}{U} = \left[1 + \left(\frac{\omega_m\left(\varphi_{wo} + \varphi_{nw} + \varphi_\sigma\right)}{\omega_m\varphi_m}\right)^2\right]^{-\frac{1}{2}} \tag{1}$$

According to Fig. 3 and (1), to increase the motor power factor, the PM flux linkage can be increased, and the armature flux linkage can be reduced. However, the motor torque is closely correlated with the PM flux linkage and the armature field working flux linkage. Therefore, to improve the power factor without affecting output torque, the PM flux linkage can be increased, while the armature field non-working flux linkage and leakage flux linkage are suppressed. Flux linkages are closely associated with magnetic density. The Fourier series expansion of the magnetic motive forces (MMFs) generated by the PMs can be expressed as (2):

$$F_{\mathrm{pm}}\left(\theta,t\right)=\sum_{k=1,3,\ldots}^{\infty}F_{\mathrm{ag}k}\cos\left(kP_{\mathrm{r}}\theta+kP_{\mathrm{r}}\omega_{\mathrm{r}}t+\theta_{\mathrm{r}k0}\right)\tag{2}$$

where k is the order of the PM MMF, P_{r} represents the PM pole-pair number, ω_{r} represents the mechanical rotational speed, $F_{\mathrm{ag}k}$ indicates the amplitude of the k-th harmonic of the MMF generated by the PMs, $\theta_{\mathrm{r}k0}$ is the initial phase angle of the k-th order MMF, θ represents the airgap circumferential position angle, and t represents a specific moment during the operation of the motor.

For the motor, the modulation teeth serve as the key element for generating harmonics in the airgap. The Fourier series expansion of its permeance function is expressed as (3):

$$\Lambda\left(\theta\right)=\Lambda_{0}+\sum_{n=1,2,3,\ldots}\Lambda_{\mathrm{n}}\cos\left(nN_{\mathrm{s}}\theta\right)\tag{3}$$

where N_{s} is the stator slot number, Λ_{n} represents the amplitude of the n-th order permeance function, and Λ_{0} represents the amplitude of the 0-th order permeance function.

Based on (2) and (3), the PM flux density B_{pm}, generated by the modulation effect of the stator teeth on the PM MMF, can be calculated and expressed as (4):

$$\begin{aligned}B_{\mathrm{pm}}\left(\theta,t\right)&=F_{\mathrm{pm}}\left(\theta,t\right)\times\Lambda\left(\theta\right)\\&=\sum_{k=1,3,\ldots}^{\infty}F_{\mathrm{ag}k}\Lambda_{0}\cos\left(kP_{\mathrm{r}}\theta+kP_{\mathrm{r}}\omega_{\mathrm{r}}t+\theta_{\mathrm{r}k0}\right)+\\&\sum_{k=1,3,\ldots}^{\infty}\sum_{n=1,2,3,\ldots}^{\infty}F_{\mathrm{ag}k}\Lambda_{n}\cos\left[kP_{\mathrm{r}}\omega_{\mathrm{r}}t+\left(kP_{\mathrm{r}}\pm nN_{\mathrm{s}}\right)\theta+\theta_{\mathrm{r}k0}\right]\end{aligned}\tag{4}$$

From (4), it can be seen that, apart from the fundamental wave of order kP_{r} (k = 1, 3, 5, …) produced by the PM MMF, harmonics of orders $|kP_{\mathrm{r}}\pm nN_{\mathrm{s}}|$ (n = 1, 2, 3, …) are generated after the modulation effect of the stator teeth on the PM MMF.

Meanwhile, the Fourier series expansion of the armature MMF (F_{aw}) is expressed as (5):

$$F_{\mathrm{aw}}\left(\theta,t\right)=\sum_{p}^{\infty}F_{\mathrm{aw}p}\cos\left(p\theta-\omega_{\mathrm{e}}t\right)+\sum_{q}^{\infty}F_{\mathrm{aw}q}\cos\left(q\theta+\omega_{\mathrm{e}}t\right)\tag{5}$$

where $F_{\mathrm{aw}p}$ and $F_{\mathrm{aw}q}$ represent the amplitudes of the p-th and q-th order harmonics of the armature MMF, and ω_{e} denotes the electrical angular velocity. It can be observed that the armature field generates fundamental components of the p-th and q-th orders.

Based on (3) and (5), the armature flux density B_{aw}, generated by the modulation effect of the stator teeth on the armature MMF, can be calculated and expressed as (6):

$$\begin{aligned}B_{\mathrm{aw}}\left(\theta,t\right)&=F_{\mathrm{aw}}\left(\theta,t\right)\times\Lambda\left(\theta\right)\\&=\sum_{p}^{\infty}F_{\mathrm{aw}p}\Lambda_{0}\cos\left(p\theta-\omega_{\mathrm{e}}t\right)+\sum_{q}^{\infty}F_{\mathrm{aw}q}\Lambda_{0}\cos\left(q\theta+\omega_{\mathrm{e}}t\right)+\\&\sum_{p}^{\infty}\sum_{n=1,2,3\ldots}^{\infty}\frac{1}{2}F_{\mathrm{aw}p}\Lambda_{n}\cos\left[\left(p\pm kN_{\mathrm{s}}\right)\theta-\omega_{\mathrm{e}}t\right]+\\&\sum_{q}^{\infty}\sum_{n=1,2,3\ldots}^{\infty}\frac{1}{2}F_{\mathrm{aw}q}\Lambda_{n}\cos\left[\left(q\pm kN_{\mathrm{s}}\right)\theta+\omega_{\mathrm{e}}t\right]\end{aligned}\tag{6}$$

From (6), it can be seen that, apart from the fundamental wave produced by the armature MMF, harmonics of orders $|p\pm kN_{\mathrm{s}}|$ and $|q\pm kN_{\mathrm{s}}|$ are generated after the modulation effect of the stator teeth on the armature MMF.

The PM flux linkage is determined by the PM flux density and the motor structure, and can be expressed as (7):

$$\begin{aligned}\varphi_{\mathrm{m}}\left(t\right)&=rln_{\mathrm{c}}\int_{-\pi/N_{\mathrm{s}}}^{\pi/N_{\mathrm{s}}}B_{\mathrm{pm}}\left(\theta,t\right)\mathrm{d}\theta\\&=\sum_{k=1,3,\ldots}^{\infty}F_{\mathrm{ag}k}\Lambda_{0}\frac{2rln_{\mathrm{c}}}{kP_{\mathrm{r}}}\sin\frac{\pi kP_{\mathrm{r}}}{N_{\mathrm{s}}}\cos\left(kP_{\mathrm{r}}\omega_{\mathrm{m}}t+\theta_{\mathrm{r}k0}\right)+\\&\sum_{k=1,3,\ldots}^{\infty}\sum_{n=1,2,3,\ldots}^{\infty}\frac{F_{\mathrm{ag}k}\Lambda_{n}}{2}\frac{2rln_{\mathrm{c}}}{kP_{\mathrm{r}}\pm nN_{\mathrm{s}}}\sin\frac{\pi(kP_{\mathrm{r}}\pm nN_{\mathrm{s}})}{N_{\mathrm{s}}}\cos\left(kP_{\mathrm{r}}\omega_{\mathrm{m}}t+\theta_{\mathrm{r}k0}\right)\end{aligned}\tag{7}$$

where r is the airgap radius, l is the axial length, and n_{c} represents the turn number of windings. For the PM flux linkage, only its fundamental component contributes to the average torque. From (7), it can be seen that the fundamental component of the PM flux linkage is obtained when k is equal to 1. Its amplitude (ψ_{m}) can be expressed as (8):

$$\begin{aligned}\psi_{\mathrm{m}}&=F_{\mathrm{ag1}}\Lambda_{0}\frac{2rln_{\mathrm{c}}}{P_{\mathrm{r}}}\sin\frac{\pi P_{\mathrm{r}}}{N_{\mathrm{s}}}\cos\left(\theta_{\mathrm{r}k0}\right)+\\&\sum_{n=1,2,3,\ldots}^{\infty}\frac{F_{\mathrm{ag1}}\Lambda_{n}}{2}\frac{2rln_{\mathrm{c}}}{P_{\mathrm{r}}\pm nN_{s}}\sin\frac{\pi(P_{\mathrm{r}}\pm nN_{\mathrm{s}})}{N_{\mathrm{s}}}\cos\left(\theta_{\mathrm{r}k0}\right)\end{aligned}\tag{8}$$

Similarly, the armature flux linkage (φ_{aw}) can be expressed as (9):

$$\begin{aligned}\varphi_{\mathrm{aw}}\left(t\right)&=rln_{\mathrm{c}}\int_{-\pi/N_{\mathrm{s}}}^{\pi/N_{\mathrm{s}}}B_{\mathrm{aw}}\left(\theta,t\right)\mathrm{d}\theta\\&=\sum_{p}^{\infty}F_{\mathrm{aw}p}\Lambda_{0}\frac{2rln_{\mathrm{c}}}{p}\sin\frac{\pi p}{N_{\mathrm{s}}}\cos\omega_{\mathrm{e}}t+\\&\sum_{q}^{\infty}F_{\mathrm{aw}q}\Lambda_{0}\frac{2rln_{\mathrm{c}}}{q}\sin\frac{\pi q}{N_{\mathrm{s}}}\cos\omega_{\mathrm{e}}t+\\&\sum_{p}^{\infty}\sum_{n=1,2,3\ldots}^{\infty}F_{\mathrm{aw}p}\Lambda_{n}\frac{rln_{\mathrm{c}}}{p\pm kN_{\mathrm{s}}}\sin\frac{\pi p}{N_{\mathrm{s}}}\cos\omega_{\mathrm{e}}t+\\&\sum_{q}^{\infty}\sum_{n=1,2,3\ldots}^{\infty}F_{\mathrm{aw}q}\Lambda_{n}\frac{rln_{\mathrm{c}}}{q\pm kN_{\mathrm{s}}}\sin\frac{\pi q}{N_{\mathrm{s}}}\cos\omega_{\mathrm{e}}t\end{aligned}\tag{9}$$

All harmonics of the armature field contribute to the amplitude of the fundamental component of the armature flux linkage. Its amplitude can be expressed as (10):

$$\begin{aligned}\psi_{\mathrm{aw}}&=\sum_{p}^{\infty}F_{\mathrm{aw}p}\Lambda_{0}\frac{2rln_{\mathrm{c}}}{p}\sin\frac{\pi p}{N_{\mathrm{s}}}+\\&\sum_{q}^{\infty}F_{\mathrm{aw}q}\Lambda_{0}\frac{2rln_{\mathrm{c}}}{q}\sin\frac{\pi q}{N_{\mathrm{s}}}+\\&\sum_{p}^{\infty}\sum_{n=1,2,3\ldots}^{\infty}F_{\mathrm{aw}p}\Lambda_{n}\frac{rln_{\mathrm{c}}}{p\pm kN_{\mathrm{s}}}\sin\frac{\pi p}{N_{\mathrm{s}}}+\\&\sum_{q}^{\infty}\sum_{n=1,2,3\ldots}^{\infty}F_{\mathrm{aw}q}\Lambda_{n}\frac{rln_{\mathrm{c}}}{q\pm kN_{\mathrm{s}}}\sin\frac{\pi q}{N_{\mathrm{s}}}\end{aligned}\tag{10}$$

According to classic motor theory, the output torque T generated by this motor can be given by the stress tensor method:

$$T=\frac{\pi r^{2}l}{\mu_{0}}B_{\mathrm{r}}B_{\mathrm{t}}\cos\left(\theta_{\mathrm{r}}-\theta_{\mathrm{t}}\right)\tag{11}$$

where μ_{0} is the vacuum permeability; B_{r} and B_{t} are the radial and tangential amplitudes of the airgap harmonics; θ_{r} and θ_{t} represent the radial and tangential phase angles of the airgap harmonics. For airgap harmonics, only radial and tangential flux density harmonics with identical pole-pair numbers and identical rotational speed can interact to generate torque.

Under the $I_d = 0$ control strategy for the motor, the relationship between the inductance and flux linkage is expressed as (12) [32]:

$$L_0 = \frac{\varphi}{I} \tag{12}$$

where φ denotes the armature flux linkage, L_0 denotes the inductance, and I denotes the root mean square of the phase current. The power factor formula can also be expressed as (13) [33]:

$$\cos\theta_p = \left[1 + \left(\frac{L_0 I}{\varphi_m}\right)^2\right]^{-\frac{1}{2}} \tag{13}$$

where φ_m denotes the PM flux linkage. It is noteworthy that the inductance corresponds to the armature field. As indicated by the preceding analysis, the armature working flux linkage and non-working flux linkage are closely related to the armature harmonics. Through targeted suppression of the non-working armature harmonics, the non-working armature flux linkage can be suppressed. Consequently, the inductance L_0 will also be reduced, leading to an improvement in the power factor of the motor [27].

Based on analysis of the PM and armature fields, it is determined that the 4th, 14th, and 32nd harmonics can generate torque and provide the fundamental component of the PM flux linkage. These are defined as working harmonics. For the armature field, the 4th, 14th, and 32nd harmonics interact with corresponding harmonic orders of the PM magnetic field to produce torque. The 2nd, 6th, 8th, 12th, 30th, and other harmonics of the armature field contribute no torque but degrade the power factor; these are defined as non-working harmonics. The enhancement of the working harmonics is beneficial for increasing the PM flux linkage, thereby improving the back-EMF amplitude E_0, as shown in Fig. 3. The harmonic classifications for both PM and armature fields are summarized in Table I.

TABLE I
CLASSIFICATION OF WORKING AND NON-WORKING HARMONICS IN PM AND ARMATURE FIELDS

Items		Harmonic order
PM field	Working harmonics	4, 14, and 32
	No-working harmonics	—
Armature field	Working harmonics	4, 14, and 32
	No-working harmonics	2, 6, 8, 12, and 30

Based on the previous analysis of the PM field and armature field, the mechanism for improving output torque and power factor is summarized from the perspective of these two fields, as illustrated in Fig. 4. The upper section corresponds to the PM field harmonic region. For working harmonics in this region, their amplitude is closely related to torque and PM flux linkage. Enhancing the amplitude of torque-contributing harmonics facilitates the improvement of output torque from the PM field. This enhancement also increases the PM flux linkage, which contributes to improved power factor. The lower section corresponds to the armature field harmonic region. As analyzed in Fig. 3, enhancing the amplitude of working harmonics in the armature field increases the working flux linkage of the armature, thereby improving output torque from the armature field. For non-working harmonics of the armature field, suppressing their amplitude reduces the non-working flux linkage of the armature and also decreases the inductance L_0, which enhances the power factor without affecting the output torque.

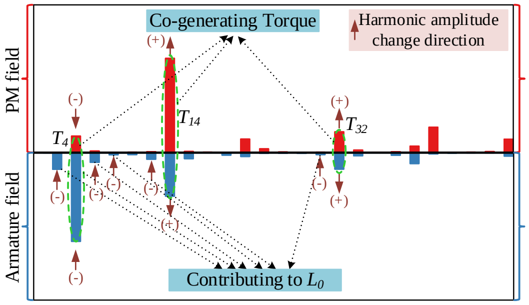

Fig. 4. Analysis of the synergistic improvement mechanism of power factor and torque based on the harmonics of PM and armature fields.

III. POWER FACTOR IMPROVEMENT DESIGN

Based on the analysis in Section II, the relationships between power factor and flux linkage, as well as between flux linkage and harmonics, were examined. This analysis clarified the direction for improving motor power factor through harmonic optimization. This section investigates the influence of variations in two key elements (magnetic source and permeance) on critical harmonics. Targeted improvement of key harmonics affecting power factor and torque is conducted, ultimately achieving enhanced performance.

A. *Design of PM Topology*

Based on prior analysis, improving the motor power factor can be addressed from both the PM field and the armature field. For the PM field, enhancing its PM flux linkage elevates motor torque and power factor, where the PM flux linkage is closely related to MMF. As established earlier, the 14th harmonic constitutes the fundamental component of the PM field. The arrangement of PMs directly influences the distribution of PM MMF. Harmonic magnetic circuit analysis of the 14th harmonic facilitates the pursuit of an optimal PM configuration. The equivalent magnetic circuit models for the 14th harmonic under different PM topologies are shown in Fig. 5. From Fig. 5(a), it can be observed that the equivalent magnetic circuit of the V-shaped PMs is arranged in series. For the Y-shaped PMs in Fig. 5(b), the upper V-shaped PMs retain the series magnetic circuit while forming a parallel magnetic circuit with the lower V-shaped PMs. This configuration creates multi-flux paths, improving PM utilization and reducing end leakage flux. Moreover, the arrangement parameters of PMs are closely related to airgap flux density harmonics. Therefore, selecting appropriate arrangements contributes to improved harmonic amplitudes and enhanced motor performance.

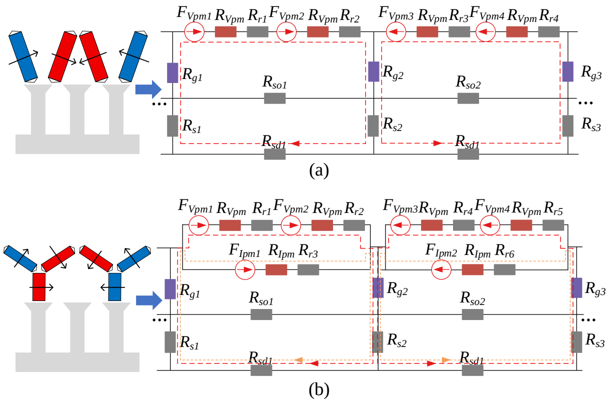

(b)

Fig. 5. The equivalent magnetic circuits of the 14th harmonic with different PM topologies. (a) V-shaped PMs and their magnetic circuits. (b) Y-shaped PMs and their magnetic circuits.

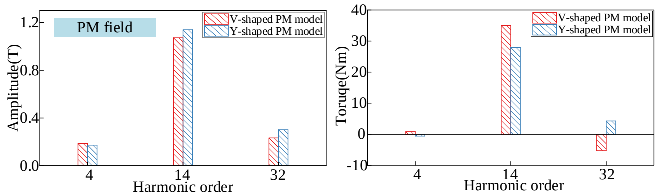

(a) (b)

Fig. 6. Comparison of harmonics and torques in different PM topologies. (a) Harmonic amplitude. (b) Harmonics contribute to torque.

The amplitude of torque-related harmonics and corresponding torque contributions under two PM topologies are shown in Fig. 6. It can be observed that the Y-shaped PMs facilitate enhancement of both the fundamental wave and its first-order modulated 32nd harmonic, beneficial for increasing the amplitude of the fundamental component of the PM flux linkage and improving motor power factor. Additionally, as the PM structure shifts from V-shaped to Y-shaped, although the torque contributed by the 14th harmonic decreases somewhat, the torque contributed by the 32nd harmonic changes from negative to positive. Overall, the torque contributed by harmonics is further increased.

A comparison of flux linkage under two PM topologies is shown in Fig. 7. It can be observed that the Y-shaped topology exhibits higher flux linkage, beneficial for simultaneous improvement of power factor and torque. Analysis from perspectives of the magnetic circuit and harmonics indicates that the Y-shaped PMs offer greater advantages for motor performance improvement compared to the V-shaped topology. Therefore, the Y-shaped PMs are selected as the object for subsequent analysis.

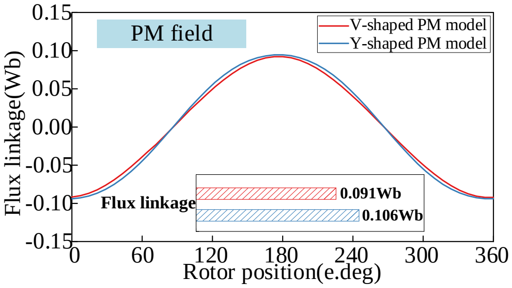

Fig. 7. Comparison of flux linkage under different PM topologies.

The structural parameters of PMs are closely related to airgap harmonic distribution. To achieve superior PM field distribution, the structural parameters of Y-shaped PMs are shown in Fig. 8. Key parameters include the I-shaped PM length L_{pm1}, V-shaped PM length L_{pm2}, V-shaped PM tilt angle β_{pm1}, relative horizontal position between V-shaped and I-shaped magnets M_{1x}, relative vertical position between V-shaped and I-shaped magnets M_{1y}, horizontal dimension of triangular magnetic barriers M_{bx}, and vertical dimension of triangular magnetic barriers M_{by}.

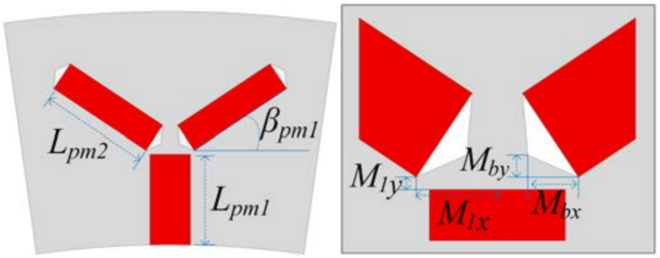

(a) (b)

Fig. 8. Parametric model of Y-shaped PM structure. (a) PM structure. (b) Partial PM structure parameters.

Based on the previous analysis, the 14th harmonic serves as the fundamental wave, whose amplitude significantly influences torque and power factor. Therefore, the amplitude of this harmonic is selected as the analysis subject.

Through response surface analysis, the impact of various PM structural parameters on the 14th harmonic is illustrated in Fig. 9. The figure reveals that structural parameters exhibiting a positive correlation with the 14th harmonic amplitude include L_{pm2} and M_{1x}, while those demonstrating a negative correlation include L_{pm1}, β_{pm1}, and M_{1y}. According to the response surface analysis results, the reasonable selection ranges for each parameter are summarized in Table II. The final structural parameters are determined in conjunction with permeance design to establish a rational airgap harmonic distribution.

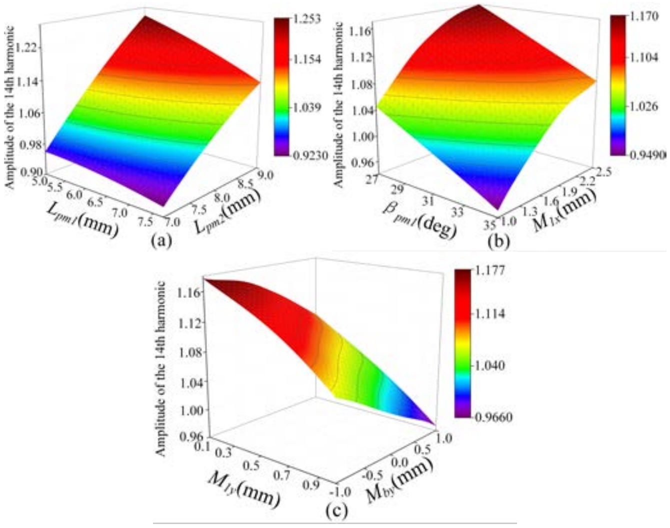

Fig. 9. Analysis of the response surface of different PM structural parameters to the 14th harmonic amplitude. (a) L_{pm1}, L_{pm2}, and the 14th harmonic amplitude. (b) β_{pm1}, M_{1x}, and the 14th harmonic amplitude. (c) M_{1y}, M_{by}, and the 14th harmonic amplitude.

TABLE II
INITIAL VALUES AND RANGES OF PM STRUCTURAL PARAMETERS

Item	Initial value	Range
L_{pm1}/mm	6.61	[6.5, 7.6]
L_{pm2}/mm	8.08	[8, 9]
β_{pm1}/(º)	33.67	[29, 34]
M_{1x}/mm	1.76	[1.2, 2]
M_{1y}/mm	0.27	[0.2, 0.6]
M_{bx}/mm	1.1	[0.8, 1.2]
M_{by}/mm	0.48	[−0.5, 0.5]

B. *Design of Permeance*

Permeance, as one of the three essential elements for magnetic field modulation, exerts a critical influence on magnetic field harmonics. This section will suppress the non-working harmonics of the armature field from the perspective of permeance. Analysis based on (4), (6), and Table I reveals that the non-working harmonics of order 2, 6, 8, 12, and 30 in the armature field are modulated by Λ_0. The working harmonics of order 4 and 32 in the armature field are also modulated by Λ_0, while the 14th harmonic results from the combined modulation of Λ_0 and Λ_1 of the 4th harmonic. Therefore, appropriately suppressing Λ_0 favors the suppression of non-working armature flux linkage. Simultaneously, analysis in Fig. 6 indicates the 4th harmonic contributes negative torque; suppression of Λ_0 thus favors torque improvement. For the working harmonics in the PM field, the 14th harmonic is modulated by Λ_0, while the 4th and 32nd harmonics are modulated by Λ_1. However, weakening Λ_0 will also reduce the 14th harmonic in the PM field, which is detrimental to torque improvement. Notably, the 32nd harmonic of the PM field contributes a portion of positive torque; this harmonic and the 14th harmonic of the armature field are both modulated by Λ_1. Consequently, appropriately weakening Λ_0 while enhancing the amplitude of Λ_1 facilitates improvement of the motor power factor without sacrificing torque. The permeance analysis findings are summarized in Table III.

TABLE III
CLASSIFICATION OF PM AND ARMATURE FIELD HARMONICS WITH CORRESPONDING PERMEANCE

Items		Harmonic order	Permeance order
PM field	Working harmonics	4 and 32	1
		14	0
Armature field	Working harmonics	4 and 32	0
		14	0 and 1
	No-working harmonics	2, 6, 8, 12, and 30	0

The permeance modulation function is intrinsically related to stator tooth-shaped design parameters, including stator tooth width A_x, stator shoe length A_y, and stator shoe angle R_{ws}. Structured parameters of the stator tooth are given in Fig. 10. Through design adjustments to these tooth parameters, targeted improvement of specific harmonic orders of permeance can be achieved, thereby influencing armature field harmonics. Details of the initial model, parameter ranges, and final model for the stator tooth structural parameters are provided in Table IV.

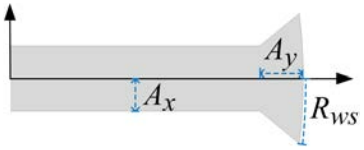

Fig. 10. Structured parameters of stator teeth.

TABLE IV
INITIAL VALUES, RANGES, AND OPTIMAL VALUES OF STATOR TOOTH STRUCTURAL PARAMETERS

Item	Initial value	Range	Optimal value
R_{ws}/(º)	7.12	[5, 7.5]	5.6
A_y/mm	5.74	[3.3, 7.3]	5.3
A_x/mm	4.29	[3.5, 5]	4.2

The sensitivity of stator tooth structural parameters to permeance harmonics can be calculated using (14):

$$\rho\left(X_i, Y_i\right)=\frac{N\sum X_iY_i-\sum X_i\sum Y_i}{\sqrt{N\sum X_i^2-\left(\sum X_i\right)^2}\sqrt{N\sum Y_i^2-\left(\sum Y_i\right)^2}} \quad (14)$$

where N is the sample number, X_i is the i-th design parameter, and Y_i is the optimization objective.

The sensitivity of stator tooth structural parameters to Λ_0 and Λ_1 is illustrated in Fig. 11. Regarding Λ_0, A_x and R_{ws} exhibit high sensitivity. For Λ_1, R_{ws} demonstrates high sensitivity. Based on the requirements for suppressing Λ_0 and enhancing Λ_1, the selected stator tooth structural parameters are presented in Table III. Based on the sensitivity of different stator structures to permeance harmonics, an appropriate stator structure is selected to achieve a slight decrease of Λ_0 and a significant increase of Λ_1.

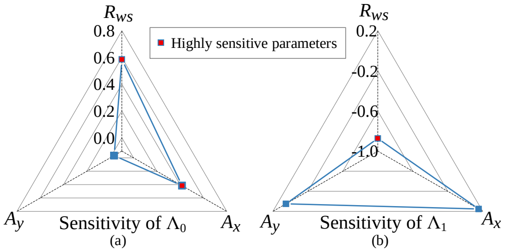

(a) (b)

Fig. 11. Sensitivity analysis of stator structural parameters to permeance harmonics. (a) Sensitivity of Λ_0. (b) Sensitivity of Λ_1.

For the stator tooth structural parameters, the permeance waveform can be calculated through conformal mapping method [34]-[35]. Comparisons of permeance waveforms before and after stator tooth structural adjustment are presented in Fig. 12. It can be observed from Fig. 12(b) that after stator tooth modification, Λ_0 slightly decreases while Λ_1 significantly increases. This facilitates improvement of the motor power factor without sacrificing torque. Stator tooth design thus enables the intended adjustments to permeance harmonics.

The harmonic variations of the PM and armature fields before and after stator tooth improvement are compared in Fig. 13. As shown in Fig. 13(a), stator tooth design reduces Λ_0, thereby decreasing non-working harmonics in the armature field, specifically the 6th, 8th, 12th, and 30th harmonic orders. This reduces non-working flux linkage and

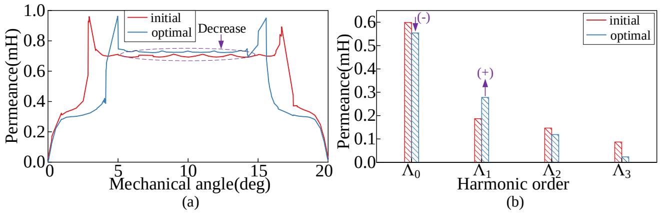

Fig. 12. Comparison of permeance waveforms and permeance harmonics before and after stator tooth design. (a) Permeance waveforms. (b) Permeance harmonics.

improves power factor. Simultaneously, the reduction of Λ_0 lowers the 4th harmonic of the armature field, thereby reducing its negative torque contribution. Conversely, enhancing Λ_1 increases the amplitudes of the 14th harmonic in the armature field and the 32nd harmonic in the PM magnetic field, consequently improving output torque.

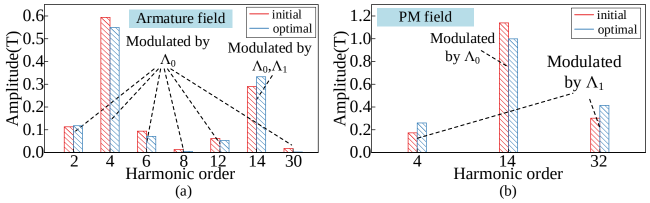

Fig. 13. The changes in harmonic modulation effects of armature and PM fields before and after permeance design. (a) Harmonic changes of armature field. (b) Harmonic changes of PM field.

C. *Optimization of PM Topology*

After stator tooth design, the three essential components of the motor are the magnetic source, permeance, and filter element. Among these, permeance can be adjusted to regulate harmonics to meet design requirements. This allows the motor power factor to be improved as much as possible while maintaining motor torque. Subsequently, through parameter design of the Y-shaped PM structure, the amplitude of the 14th harmonic is enhanced to achieve optimal output torque.

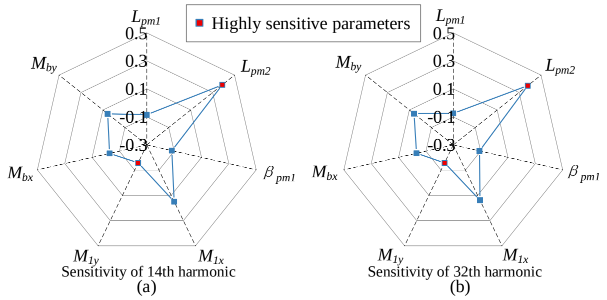

Fig. 14. Sensitivity analysis of PM structural parameters to the amplitudes of the 14th and 32nd harmonics. (a) 14th harmonic sensitivity. (b) 32nd harmonic sensitivity.

Analysis from Fig. 6 indicates that both the 14th and 32nd harmonics contribute positive torque. Therefore, the amplitude of the 32nd harmonic is also considered as an analysis target. Sensitivity analysis of PM structural parameters on the amplitudes of the 14th and 32nd harmonics is presented in Fig. 14. Results demonstrate that L_{pm2} and M_{1y} are highly sensitive parameters for both harmonics. These two parameters can be regarded as common design variables for both harmonics.

The response surface analysis for highly sensitive parameters regarding the 14th harmonic is shown in Fig. 15. The optimized design was selected from candidate points. Optimized PM structural parameters are summarized in Table V.

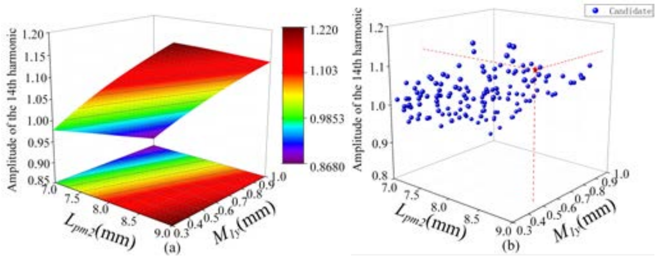

Fig. 15. The high-sensitivity parameters of PM structure to the 14th harmonic response surface, feasible design points, and final design point. (a) Amplitude of the 14th harmonic response surface for highly sensitive parameters. (b) Feasible design points and final selection point.

TABLE V
INITIAL AND FINAL VALUES OF STATOR TOOTH STRUCTURAL PARAMETERS

Item	Initial value	Optimal value
L_{pm1}/mm	6.61	7.5
L_{pm2}/mm	8.08	8.85
β_{pm1}/(°)	33.67	30
M_{1x}/mm	1.76	1.3
M_{1y}/mm	0.27	0.5
M_{bx}/mm	1.1	1
M_{by}/mm	0.48	0

To enhance the rigor of the paper, the main parameters of the motor structure are provided in Table VI as follows.

TABLE VI
KEY DESIGN PARAMETERS

Item	Value
Rated power/kW	1.7
Rated speed/(r·min^{-1})	400
Rotor outer diameter/mm	174
Rotor inner diameter/mm	140
Stator outer diameter/mm	138.6
Stator inner diameter/mm	42
Pole pair number of rotor	14
Number of stator slots	18
Pole pair number of winding	4
Coil span	2
Stack length/mm	50

IV. ELECTROMAGNETIC PERFORMANCE EVALUATION

To validate the improvement in power factor achieved through magnetic source and permeance modifications, a systematic comparative performance analysis was conducted between the initial V-shaped motor and the final design proposed in this section.

The back-EMF waveforms of the two models are compared in Fig. 16. Results demonstrate that the back-EMF amplitude E_0 of the final motor increased by 11.78%, verifying the enhancement of PM flux linkage through magnetic source design discussed earlier.

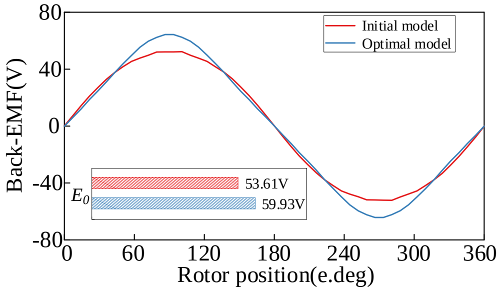

Fig. 16. Comparison of the back-EMF of two motors.

Comparative analysis of key harmonics in the armature and PM fields between the two motors is presented in Fig. 17. As shown in Fig. 17(a), magnetic source design enhances the amplitudes of PM harmonics contributing to fundamental back-EMF, which is conducive to achieving higher back-EMF and improved power factor. Simultaneously, harmonics contributing to positive torque exhibit increased amplitudes, enhancing motor torque performance. From Fig. 17(b), permeance design reduces non-working armature harmonics, namely the 6th, 8th, 12th, and 30th orders, further improving power factor. Since negative torque is contributed by the 4th harmonic, its reduction also enhances torque performance.

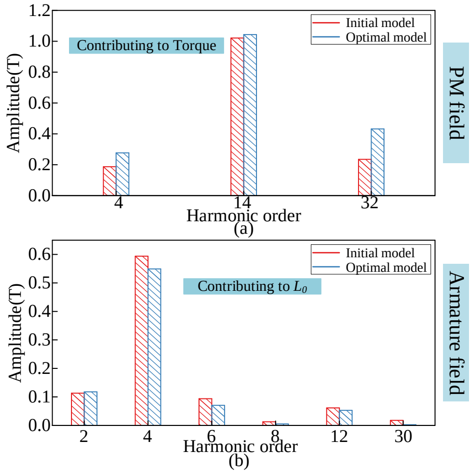

Fig. 17. Comparison of key harmonics in the PM and armature fields of the two motors. (a) Harmonics of PM field. (b) Harmonics of armature field.

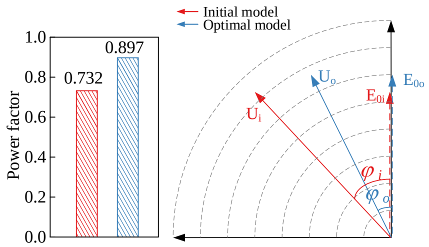

Fig. 18. Comparative analysis of power factor of two motors.

Furthermore, analysis of power factor characteristics for the two motors is presented in Fig. 18. Results demonstrate that, owing to enhanced PM flux linkage and reduced non-working flux linkage of the armature field, the power factor increased by 22.54% compared to the initial motor. This indicates that simultaneous improvements in both PM and armature fields prove more effective for enhancing power factor.

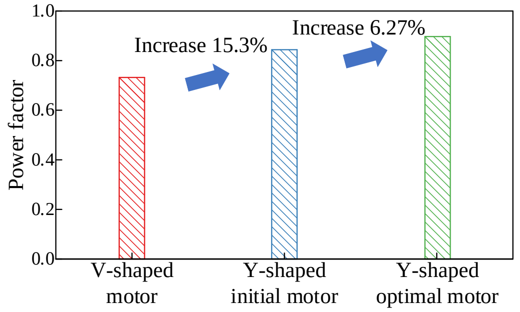

Fig. 19. Comparison of power factor across different machines.

Furthermore, Fig. 19 presents the power factors corresponding to different motor topologies. It can be observed that the transition from the V-shaped to the Y-shaped PM structure contributes to a 15.3% improvement in the machine power factor, owing to the enhancement in the PM flux linkage. Through modifications in permeance and optimization of the PM structure, which collectively improve both the PM flux linkage and the armature flux linkage, the machine power factor is further increased by 6.27%.

Comparative analysis of the torque is demonstrated in Fig. 20. After implementing PM magnetic source design, output torque increased by 17.6% compared to the initial V-shaped topology, resulting from enhanced amplitudes of harmonics contributing positive torque.

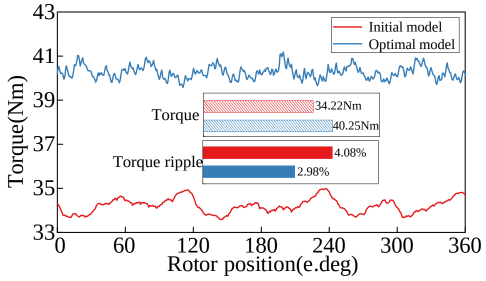

Fig. 20. Comparison of the output torques of the two motors.

V. EXPERIMENTAL VALIDATION

A 1.7 kW prototype of the Y-shaped PM motor was fabricated to validate the analysis, as displayed in Fig. 21. The figure shows the rotor, stator, and windings of the motor.

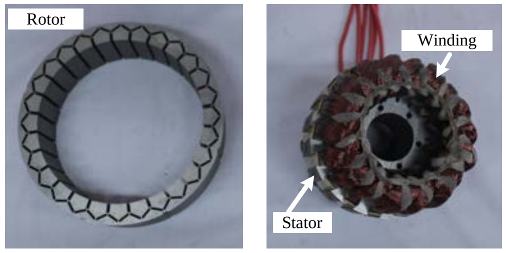

(a) (b)

Fig. 21. Y-shaped motor prototype. (a) Rotor structure. (b) Stator and winding structure.

The experimental setup for the motor is established concurrently, shown in Fig. 22, primarily comprising three components: experimental platform, data recorder, and control system.

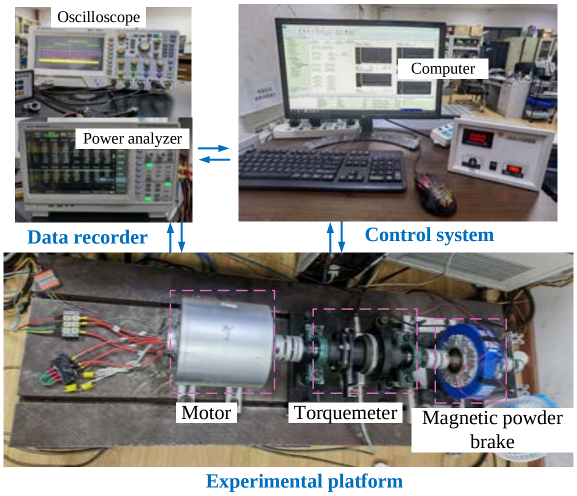

Fig. 22. Motor experiment platform.

The fundamental performance test results of the motor are presented in Fig. 23. While Fig. 23(a) displays the back-EMF waveform at 400 r/min, test results align with simulation data in Fig. 17; this confirms the validity of motor design. Fig. 23(b) demonstrates steady-state operational characteristics. Under the rated load torque of 40 N·m, stable motor operation was maintained, evidencing robust load capability.

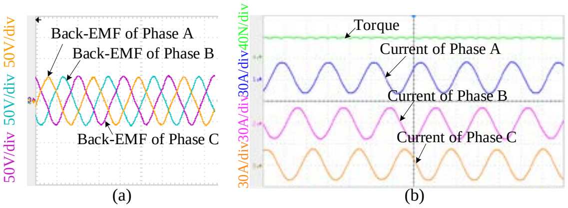

Fig. 23. The basic motor performance of the experimental test. (a) Back-EMF of the motor. (b) Steady-state torque waveform diagram of the motor.

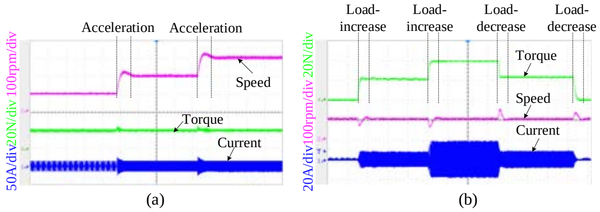

Fig. 24. Dynamic characteristic waveform of the motor. (a) Constant speed variable load test. (b) Constant load variable speed test.

Dynamic response performance of the proposed motor is further investigated through waveforms depicted in Fig. 24. As shown in Fig. 24(a), with a 20 N·m load torque, motor speed increases from 100 to 200 r/min and finally stabilizes at 300 r/min. Fig. 24(b) presents load torque variations at a constant 100 r/min speed, stepping from 0 to 20 N·m, then to 40 N·m, back to 20 N·m, and finally to 0 N·m. Stable operation is maintained throughout dynamic processes, demonstrating excellent dynamic characteristics that meet drive requirements.

The comparative analysis of the motor performance under different currents in both simulation and experiment is presented in Fig. 25. It can be observed from Fig. 25 that the torque increases while the power factor decreases with increasing current. When the motor reaches the rated current of 20 A, the simulated motor torque and power factor are 40.25 N·m and 0.897, respectively. The torque and power factor obtained from the experiment are 38.78 N·m and 0.867. The deviation between simulation and experimental results remains within an acceptable range, which verifies the effectiveness of the collaborative design method for motor performance improvement.

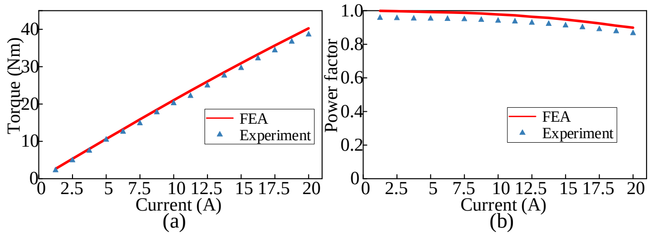

Fig. 25. Comparison of motor simulation and experimental performance under different currents. (a) Comparison of torque performance. (b) Comparison of power factor performance.

VI. CONCLUSION

This paper proposes a collaborative design method for enhancing the power factor and torque of motor, employing a Y-shaped PM vernier motor. Its core principle involves targeted harmonic design through the magnetic source and permeance, thereby coordinating improvements to the PM flux linkage and armature flux linkage. The main research findings are summarized as follows:

1) The relationship between the power factor and flux linkage is established from the PM and armature field. The connection between flux linkage and harmonics is constructed. The coordinated enhancement of PM and armature flux linkages through harmonic improvement is clarified, determining the direction for improving power factor and torque.

2) Through magnetic circuit analysis, the Y-shaped PM structure enhances the PM flux linkage and increases the amplitude of torque-producing harmonics. A rational design range for the PM structure is provided.

3) Collaborative design of specific permeance harmonic orders suppresses the non-working flux linkage of the armature field while enhancing its torque-producing harmonic flux linkage. This improves the motor power factor while maintaining torque. PM structure design optimizes the motor torque performance. Compared to the initial design, the optimized motor achieved 22.54% improvement in power factor and 18.6% torque increase.

Finally, a prototype of the optimized Y-shaped PM vernier motor was constructed. Experimental testing largely validated the effectiveness of the proposed PM and permeance design methodology. This approach offers a viable and effective solution for enhancing power factor and torque in PM vernier motor.

REFERENCES

[1] L. Fang, D. W. Li, and R. H. Qu, “Torque Improvement of Vernier Permanent Magnet Machine with Larger Rotor Pole Pairs than Stator

Teeth Number," *IEEE Trans. on Ind. Electron*., vol. 70, no. 12, pp. 12648–12659, Dec. 2023.

[2] Z. X. Xiang, Y. T. Zhou, and X. Y. Zhu *et al*., "Research on Characteristic Airgap Harmonics of a Double-rotor Flux-modulated PM Motor based on Harmonic Dimensionality Reduction," *IEEE Trans. on Transp. Electrif*., vol. 10, no. 3, pp. 5750–5761, Sept. 2024.

[3] Z. P. Wu, L. Quan, and Z. X. Xiang *et al*., "Airgap-harmonic-oriented Partitioned Design Method of PMV Motor with Improved Torque Performances," *CES Trans. on Elect. Mach. and Syst*., vol. 8, no. 1, pp. 43–50, Mar. 2024.

[4] Y. H. Sun, W. X. Zhao, and J. H. Ji *et al*., "Overview of Multi-star Multi-phase Permanent Magnet Machines with High Torque Performance and Its Key Technologies," *Trans. of China Electrotechn. Soc*., vol. 38, no. 6, pp. 1403–1420, Mar. 2023.

[5] X. K. Zhu, C. H. Song, and M. Cheng *et al*., "Coordinate Transformation based on Vector Magnetic Circuit Theory and Its Application in Sensorless Control of SPMSM," *IEEE Trans. on Ind. Electron.*, pp. 1–11, Dec. 2025.

[6] X. K. Zhu, D. J. Zhao, and M. Cheng *et al*., "Mathematical Model and Vector Control of SPMSM Considering Eddy Current and Hysteresis Effects based on Vector Magnetic Circuit Theory," *IEEE Trans. on Power Electron.*, pp. 1–9, Nov. 2025.

[7] Z. X. Xiang, J. Q. Wei, and X. Y. Zhu, "Torque Ripple Suppression of a PM Vernier Machine from Perspective of Time and Space Harmonic Magnetic Field," *IEEE Trans. on Ind. Electron*., vol. 71, no. 9, pp. 10150–10161, Sept. 2024.

[8] C. B. Li, X. H. Wang, and F. Liu *et al*., "Analysis of Permanent Magnet-assisted Synchronous Reluctance Motor based on Equivalent Reluctance Network Model," *CES Trans. on Elect. Mach. and Syst*., vol. 6, no. 2, pp. 135–144, Jun. 2022.

[9] L. Fang, D. W. Li, and X. Ren *et al*., "A Novel Permanent Magnet Vernier Machine with Coding-shaped Tooth," *IEEE Trans. on Ind. Electron.*, vol. 69, no. 6, pp. 6058–6068, Jun. 2022.

[10] X. K. Zhu, Y. B. Liu, and M. M. Li *et al*., "Design, Analysis and Test of the Dual Three-phase Permanent Magnet Vernier Superconducting Armature Electrical Machine Prototype", *Supercond. Sci. Technol*., vol. 38, no. 12, pp. 125031, Dec. 2025.

[11] L. Zhang, X. Q. Li, and X. Y. Zhu *et al*., "Design and Optimization of a Five-phase Reverse-salient Fault-tolerant Permanent Magnet Motor for Electric Vehicles," *IEEE Trans. on Ind. Electron*., vol. 72, no. 7, pp. 6762–6774, Jul. 2025.

[12] X. Ren, D. W. Li, and R. H. Qu *et al*., "Investigation of Spoke Array Permanent Magnet Vernier Machine with Alternate Flux Bridges," *IEEE Trans. on Energy Convers*., vol. 33, no. 4, pp. 2112–2121, Dec. 2018.

[13] L. Fang, Y. Z. Zhang, and D. W. Li *et al*., "High-torque Density and Low-torque Ripple- Oriented Design Method for Multi-harmonics Surface-mounted PM Vernier Machine," *IEEE Trans. on Ind. Appli*., vol. 61, no. 3, pp. 3687–3700, May-Jun. 2025.

[14] L. Zhang, M. Zhang, and X. Y. Zhu *et al*., "Space Decoupling Sensorless Control of Five-phase Flux-intensifying PM Motor based on AFCCF-SMO Considering Flux-weakening Operation," *IEEE Trans. on Ind. Electron*., vol. 72, no. 7, pp. 6865–6875, Jul. 2025.

[15] M. Liao, T. Sen, and Y. Elasser *et al*., "UAV Fleet Charging on Telecom Towers with Differential Capacitive Wireless Power Transfer," *IEEE Trans. on Power Electron*., vol. 40, no. 4, pp. 6370–6384, Apr. 2025.

[16] Y. J. Shi, and T. W. Ching, "Power Factor Analysis of Dual-stator Permanent Magnet Vernier Motor with Consideration on Turn-number Assignment of Inner and Outer Stator Windings," *IEEE Trans. on Magn*., vol. 57, no. 2, pp. 1–5, Feb. 2021.

[17] Z. H. Zhang, Q. K. Han, and X. P. Xu *et al.*, "Air Gap Magnetic Field Calculation of Permanent Magnet Direct Drive Generator based on Conformal Mapping and Magnetic Equivalent Circuit Method," *Trans. of China Electrotechn. Soc.*, vol. 38, no. 3, pp. 703–711, Feb. 2023.

[18] Z. X. Xiang, Z. R. Lu, and X. Y. Zhu *et al*., "Research on Magnetic Coupling Characteristic of a Double Rotor Flux-switching PM Machine from the Perspective of Air-gap Harmonic Groups," *IEEE Trans. on Ind. Electron*., vol. 69, no. 12, pp. 12551–12563, Dec. 2022.

[19] A. Mohammadi, and S. M. Mirimani, "Design of a Novel PM-assisted Synchronous Reluctance Motor Topology Using V-shape Permanent Magnets for Improvement of Torque Characteristic," *IEEE Trans. on Energy Convers*., vol. 37, no. 1, pp. 424–432, Mar. 2022.

[20] S. S. Zhang, W. Zhang, and R. Wang *et al*., "Optimization Design of Halbach Permanent Magnet Motor based on Multi-objective Sensitivity," *CES Trans. on Elect. Mach. and Syst*., vol. 4, no. 1, pp. 20–26, Mar. 2020.

[21] Y. Zhao, D. W. Li, and X. Ren *et al*., "Low Pole-pair Ratio Integration Design of Permanent Magnet Vernier Machine with Improved Power Factor," *IEEE Trans. on Ind. Electron*., vol. 71, no. 3, pp. 2820–2830, Mar. 2024.

[22] W. X. Zhao, J. Zhu, and J. H. Ji *et al*., "Improvement of Power Factor in a Double-side Linear Flux-modulation Permanent-magnet Motor for Long Stroke Applications," *IEEE Trans. on Ind. Electron*., vol. 66, no. 5, pp. 3391–3400, May 2019.

[23] L. Xu, G. H. Liu, and W. X. Zhao *et al*., "Hybrid Stator Design of Fault-tolerant Permanent-magnet Vernier Machines for Direct-drive Applications," *IEEE Trans. on Ind. Electron*., vol. 64, no. 1, pp. 179–190, Jan. 2017.

[24] Z. Q. Zhu, and Y. Liu, "Analysis of Air-gap Field Modulation and Magnetic Gearing Effect in Fractional-slot Concentrated-winding Permanent-magnet Synchronous Machines," *IEEE Trans. on Ind. Electron*., vol. 65, no. 5, pp. 3688–3698, May 2018.

[25] D. Y. Wu, Z. X. Xiang, and X. Y. Zhu *et al*., "Optimization Design of Power Factor for an In-wheel Vernier PM Machine from the Perspective of Air-gap Harmonic Modulation," *IEEE Trans. on Ind. Electron*., vol. 68, no. 10, pp. 9265–9276, Oct. 2021.

[26] J. R. Zhou, D. Y. Fan, and Z. X. Xiang *et al*., "Production Mechanism of Power Factor of V-type Vernier Permanent Magnet Machine and Improvement Method," *Trans. of China Electrotechn. Soc.*, vol. 38, no. 14, pp. 3789–3799, Jul. 2023.

[27] T. G. Wang, X. Y. Zhu, and Z. X. Xiang *et al*., "Improvement of Power Factor and Torque of a PM Vernier Motor from Perspective of Armature and PM Field Harmonics," *IEEE Trans. on Transp. Electrif*., vol. 10, no. 3, pp. 6064–6075, Sept. 2024.

[28] L. Xu, W. J. Wu, and W. X. Zhao, "Airgap Magnetic Field Harmonic Synergetic Optimization Approach for Power Factor Improvement of PM Vernier Machines," *IEEE Trans. on Ind. Electron*., vol. 69, no. 12, pp. 12281–12291, Dec. 2022.

[29] Z. X. Xiang, W. L. Pu, and X. Y. Zhu *et al*., "Design and Analysis of a V-shaped Permanent Magnet Vernier Motor for High Torque Density," *CES Trans. on Elect. Mach. and Syst*., vol. 6, no. 1, pp. 20–28, Mar. 2022.

[30] X. Y. Zhu, M. Jiang, and Z. X. Xiang *et al*., "Design and Optimization of a Flux-modulated Permanent Magnet Motor based on an Airgap-harmonic-orientated Design Methodology," *IEEE Trans. on Ind. Electron*., vol. 67, no. 7, pp. 5337–5348, Jul. 2020.

[31] S. H. Li, C. Di, and J. W. Liu *et al*., "Inductance Calculation and Torque Analysis of Interior Permanent Magnet Synchronous Machine Considering Cross-coupling Effects," *Trans. of China Electrotechn. Soc.*, vol. 38, no. 18, pp. 4889–4899+4931, Sept. 2023.

[32] K. K. Du, L. Xu, and W. X. Zhao *et al*., "Analysis and Design of a Fault-tolerant Permanent Magnet Vernier Machine with Improved Power Factor," *IEEE Trans. on Ind. Electron*., vol. 69, no. 5, pp. 4353–4363, May 2022.

[33] Y. L. Yu, F. Chai, and Y. L. Pei *et al*., "Investigation of Power Factor Characteristic in Permanent Magnet Motors for In-wheel Direct Drive Application," *IEEE Trans. on Energy Convers.*, vol. 39, no. 3, pp. 1699–1710, Sept. 2024.

[34] W. X. Zhao, Q. Z. Hu, and J. H. Ji *et al*., "Torque Generation Mechanism of Dual-permanent-magnet-excited Vernier Machine by Air-gap Field Modulation Theory," *IEEE Trans. on Ind. Electron*, vol. 70, no. 10, pp. 9799–9810, Oct. 2023.

[35] Z. X. Xiang, S. Bi, and X. Y. Zhu *et al*., "High Torque Density and Lightweight Design of Permanent Magnet In-wheel Motor based on Magnetic Field Modulation Effect," *IEEE Trans. on Magn*., vol. 59, no. 11, pp. 1–7, Nov. 2023.

Zixuan Xiang received the B.Sc. degree from Hubei Polytechnic University, Huangshi, China, in 2010, the M.Sc. and the Ph.D. degrees in power electronics and power transmission from the School of Electrical and Information Engineering, Jiangsu University, China, in 2017.

He is currently an associate professor in School of Electrical and Information Engineering, Jiangsu University, China. His main research interests include design, optimization, and drive control of high performance permanent magnet motor and novel double mechanical port permanent magnet motor for application in modern electric vehicles and hybrid electric vehicles.

Lei Peng graduated from Jiangsu University in China in 2021 with a bachelor's degree in electrical engineering and is currently pursuing a master's degree in electrical engineering.

His current research interests include the design and analysis of flux-modulated permanent magnet machines for electric vehicles (EVs).

Xiaoyong Zhu (M'09) received the B.Sc. and M.Sc. degrees in electrical engineering from Jiangsu University, Zhenjiang, China, in 1997 and 2002, respectively, and the Ph.D. degree from the School of Electrical Engineering, Southeast University, Nanjing, China, in 2008.

He has been with Jiangsu University since 1999, where he is currently a professor with the School of Electrical Information Engineering. From 2007 to 2008, he was a research assistant with the Department of Electrical and Electronic Engineering, University of Hong Kong, Hong Kong, China. From 2012 to 2013, he was a visiting professor with the Department of Energy-Funded Graduate Automotive Technology Education Center for Electric Drive Transportation, University of Michigan, Dearborn, Michigan, USA. His current research interests include design and drive control of electric machines with wide-speed range, less rare-earth permanent magnet motor, and multi-port permanent magnet motor. In these areas, he has authored and co-authored more than 70 referred technical papers, and holds 12 patents.

Jiaqiang Wei received the B.Sc. degree in electrical engineering in 2021 from Jiangsu University, Zhenjiang, China, where he is currently working toward the Ph.D. degree in electrical engineering.

His current research interests include design and analysis of flux-modulated permanent magnet machines for electric vehicles.

Zhe Yue received the B.Sc. Electrical Engineering and Automation from Jiangsu University, Zhenjiang, China, in 2023, where He is currently working towards the M.Sc. degree in control engineering. His current research interests include the control of permanent magnet synchronous motors.